Chapter 6

Optical Polarisation

6.1 Background

One of the key features of synchrotron radiation is its high intrinsic degree of polarisation. The highest possible polarisation comes from a completely ordered $\vec{B}$ field, where the polarisation can reach $\sim 70\%$ (Longair 1994). If there is significant synchrotron emission at optical and NIR wavelengths, then one would expect to be able to detect a corresponding polarisation. Indeed, this has been used as a way to confirm the presence of synchrotron emission in optical jets. A good example was the confirmation by Baade (1956) (using photographic plates and a polaroid filter) that the optical emission from the jet of M87 was strongly polarised, and so was likely to be synchrotron emission.

Although we are primarily interested in synchrotron radiation in this thesis, we do note here that there are other methods for producing polarised light. The most common effect seen in low-luminosity AGN such as Seyferts is that of scattering or reflection from dust. The classic example is that of Seyfert 2s, such as NGC 1068 (Miller et al. 1991), that show only narrow lines in their total flux spectrum, but show broad lines in their polarised flux spectrum. This situation arises because the light from the broad line region (BLR) is obscured from the direct line of sight by a thick torus of dust and gas. Instead, light from the BLR is scattered into the line of sight by either clouds above the torus, or the inside edge of the torus itself, and, in doing so, becomes polarised. In the PHFS objects, however, the line of sight to the nucleus is not expected to pass through this torus (should one

be present in these higher luminosity objects), since flat-spectrum objects are preferentially face-on (as opposed to edge-on). Thus, we do not consider here the effect of scattering in the analysis of the polarisation.

Radio-quiet quasars generally have very little optical polarisation. The measured values are usually a few tenths of a percent, and objects with a polarisation of more than about 2% are rare (Stockman, Moore, and Angel 1984, who used the BCS, or Burbidge, Crowne, and Smith (1977) catalogue). Only about 1% of bright optically-selected quasars show high polarisation (i.e. $P > 3\%$), and these have radio and optical continua that resemble BL Lac objects. In other words, the optical emission in the high polarisation quasars seems to be due (at least in part) to a different process to that in the low polarisation objects.

The combined model used in Chapter 5 allows this possibility. It is made up of two components: a synchrotron component, which can be very highly polarised (exactly how much depends on the particle distributions and the geometry of the emitting region); and a blue power law, which represents emission from a "normal" blue quasar (most likely emission from the accretion disk). The latter component is assumed here to be unpolarised, which is a good approximation, as $P < 1\%$ for most optically-selected quasars (Antonucci 1988; Stockman et al. 1984). Hence, the degree of polarisation predicted by the modelling will be governed by the amount of synchrotron emission fit to the data. This, of course, will change with wavelength, as the proportion of total flux made up by the synchrotron emission changes.

6.2 Existing studies

The polarisation properties of quasars and blazars have been investigated previously by a number of different authors, some for samples that include some sources considered here. Wills et al. (1992) studied a large sample of bright, flat-spectrum core-dominant quasars, measuring their optical polarisation. An interesting result is that they found that the fraction of quasars with $P > 3\%$ in a fixed observed passband decreased with increasing z, possibly indicating that the percentage polarisation decreases towards shorter rest frame wavelengths. This would be consistent with the presence of a synchrotron component turning over in the optical region.

Impey and Tapia (1990) present radio and optical data for a slightly larger sample of radio-selected quasars, including optical polarisation measurements. They find strong statistical links between strong optical polarisation and properties such as compact radio structure, superluminal motion and weak emission lines (properties common to the blazar class of objects). They explain this by requiring the optical emission, as well as the compact radio emission, to be relativistically beamed. In a similar study, Impey, Lawrence, and Tapia (1991) compared VLBI structure of 50 strong radio sources with their optical properties. They found strong correlations between the strength of the unresolved core at 5GHz and optical polarisation, emission line equivalent widths and line-to-continuum ratio, and flux variability.

Smith et al. (1988) obtained multicolour ($UBVRI$) polarisation measurements of 11 highly polarised quasars, and found that three of these exhibited decreasing polarisation toward shorter wavelengths, which they modelled as a combination of polarised synchrotron emission, and two unpolarised components, from the broad-line region and the accretion disk. None of these sources, however, are part of this sample.

Finally, Smith et al. (1994) studied the optical polarisation properties of 1546+027, by using both broad band polarimetry and spectropolarimetry. They were able to decompose the optical spectrum into a polarised synchrotron component, of wavelength-independent intrinsic polarisation of 15%, and an unpolarised "LPQ" (or low-polarisation quasar – in other words, a "normal" un-polarised quasar) component (to account for the emission lines).

6.3 Optical polarisation

Firstly, we wish to compare the photometry and the predictions of the modelling with published optical polarisation measurements. We use in particular the large catalogue of measurements compiled by Wills et al. (1992). These measurements were made using a photo-multiplier tube polarimeter on the 2.1m telescope at the McDonald Observatory, in Texas, USA. The observations were taken using white light – that is, without a filter. The particular values for the polarisation that will be used are the median values of Wills et al. – these are the median of their measurements, together

with any taken from the literature (provided the errors were not too large: i.e. they excluded those with $\sigma_P > 2.4\%$). By taking the median of several observations, the resulting value is less sensitive to variability, which is a particular problem for the high-polarisation objects.

We first compare the percentage polarisation with the optical–NIR continuum slope. The values of the slope (α, where $f_\lambda \propto \lambda^\alpha$) are obtained from the fitting of the power law model to the photometry (Section 5.1). The resulting plot is shown in Fig. 6.1, together with the line of best fit (determined by linear regression). The equation of this line is $\log_{10}(P) = (0.62 \pm 0.10)\,\alpha + (1.13 \pm 0.20)$, and a correlation is present at the 99.9% confidence level (the Kendall's τ probability that a correlation is not present is 3.4×10^{-4}).

This regression line can be compared with that found by Scarpa and Falomo (1997) in their study of 73 blazars: $\log_{10}(P) = (0.40 \pm 0.08)\,\alpha + (1.40 \pm 0.10)$. We find a stronger α dependence, although the difference in the two slopes is not quite significant at the 95% level. A possible explanation for the stronger dependence on α found here is the fact that our sample contains many low polarisation and blue objects. The fact that Scarpa and Falomo consider optical indices only (as opposed to optical-NIR indices) can be discounted as an explanation, as we find a regression line slope of 0.60 ± 0.12 when the optical indices are considered instead.

It is clear from Fig. 6.1 that the redness of the optical continuum is strongly correlated with the degree of optical polarisation. This confirms the statements made about the different types of sources in Section 5.1, indicating that the optical emission in the redder sources is likely to be of a different origin to that in the blue sources. A possible explanation for the observed correlation is that the polarisation decreases with decreasing wavelength. Blue sources will then have a relatively smaller contribution from wavelengths with larger polarisations. Such a scenario is given by the model of a synchrotron component turning-over at some peak wavelength in the optical region, then decreasing rapidly – exactly what is fitted in the modelling.

We now test whether the models fit in Chapter 5 are consistent with the polarisation measurements. In other words, is the amount of polarisation related to the amount of synchrotron that is fit to the quasar's SED? This can be tested by comparing the polarisation measurements from Wills et al.

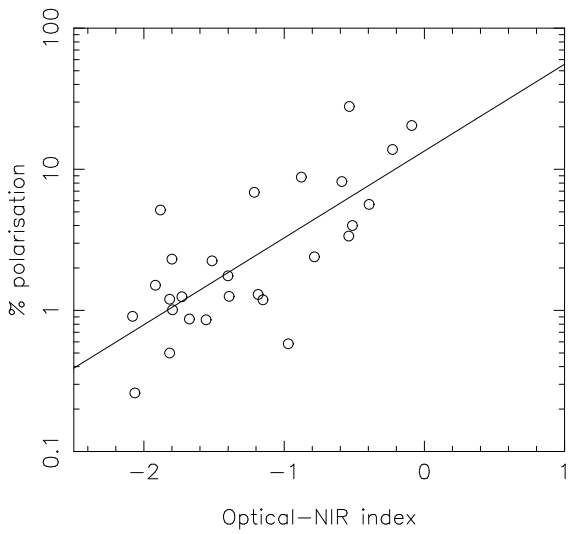

Figure 6.1: Polarisation from Wills et al. (1992) as a function of the optical-NIR spectral index, as derived from fitting the power law model in Section 5.1. The solid line is the line of best fit.

(1992) with the fractional amount of flux due to the fitted synchrotron component. However, since the observations of Wills et al. were made without a filter, the average synchrotron fraction is determined by integrating over the range 0.3μm – 1μm. This is given by

$$\langle F \rangle = \frac{\int f_S(\lambda)\,\mathrm{d}\lambda}{\int f_T(\lambda)\,\mathrm{d}\lambda}, \tag{6.1}$$

where $f_S(\lambda)$ and $f_T(\lambda)$ are the synchrotron flux and the total flux at wavelength λ.

Fig. 6.2 shows the percentage polarisation as a function of this average synchrotron fraction. For those sources that were best fit by the power law model, the fraction is calculated from the combined model fit, and these sources are indicated by a different symbol. All the power law sources with polarisation measurements had relatively red power law indices (i.e. $\alpha > -1.3$). (The bluest sources seen in Fig. 6.1 are not shown in Fig. 6.2 because they are too blue to be fit by the synchrotron model.)

The spread in polarisation measurements at large synchrotron fractions is much greater than at low fractions, indicating that the high polarisation sources generally have large amounts of synchrotron fitted to them (at the

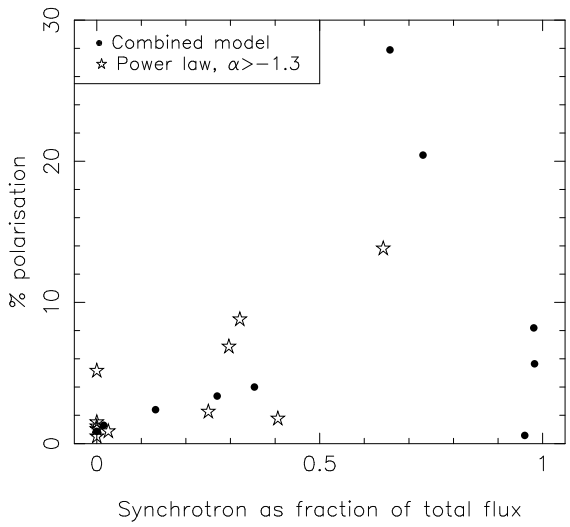

Figure 6.2: Polarisation from Wills et al. (1992) as a function of the proportion of the total flux made up by synchrotron. The sources are given different symbols according to the nature of their best fit model.

wavelengths at which the polarisation is measured). Additionally, all but one of the sources at zero (or near-zero) synchrotron fraction have low optical polarisation.

The two exceptions to this picture are 0202−172 and 1020−103. Firstly, 1020−103 has a very high synchrotron fraction ($\sim 95\%$), but has very little optical polarisation ($P = 0.58\%$). In this case, the source has a power law continuum with a slight curvature, which is fit well by an almost pure synchrotron curve (giving the high synchrotron fraction). It may be that this curvature is due to effects other than synchrotron, which would explain the lack of polarisation. A possible candidate is contamination from the very strong Hα line, which would boost the continuum level in the centre of the SED.

Secondly, 0202−172 has a measured polarisation of $P = 5.15\%$, but also has a very blue power law continuum ($\alpha = -1.85$). This continuum slope is possibly too steep to attribute to synchrotron (it implies a value of $p = 1.3$ – in turn implying a rather flat energy distribution). However, the location of the synchrotron peak may have shifted in the period since the polarisation measurements were made (the polarisation measurements were taken 8 years prior to the photometry observations).

This raises the main caveat for this sort of study. There is a long gap

in time between the polarisation measurements and the observations that obtained the photometry (which was used to derive the synchrotron fractions). The flux and polarisation of the sources may well have varied in that period, particularly for the high-polarisation sources.

6.4 Near-infrared polarisation

6.4.1 The data

To try to avoid the problem of non-simultaneity of the photometry and polarisation observations, it was decided to obtain polarisation measurements of a number of PHFS objects in the NIR, closer in time with optical photometry observations. This would enable the photometry measurements to be nearly simultaneous with the data used in the model fitting, and thus better able to predict the wavelength dependence of the polarisation from the model fitting results.

The polarisation measurements that are used in this thesis come from two observing runs on the Anglo-Australian Telescope, using the *IRIS* instrument. The first set of observations were made on the nights of February 27 – March 2, 1997, by Frank Masci, Paul Francis and the author. The sources observed were selected according to brightness in K band (from previous observations). An object with $K \sim 15$ would have required ~ 3 hours integration time, and considerably more at J band, so only sources with $K < 14$ were chosen.

The polarimetry observations and reduction are described in detail in Frank Masci's Ph.D. thesis (Masci 1997), and the results are given in Table 6.1. (Note that 1510−089 was not observed in the H band.) For all of these sources, the observations were between 41 and 49 days earlier than the optical and NIR observations from Francis et al. (2000) used for the model fitting.

Does the fact that the two sets of data are not exactly simultaneous matter? Obviously, one would prefer them to be so. However, what we are looking for here is the wavelength dependence of the polarisation, or, equivalently, the wavelength dependence of the proportional amount of synchrotron flux. The wavelength dependence itself is governed primarily by the location of the synchrotron peak (the relative normalisations of the synchrotron and power law components will affect the normalisation of the polarisation

curve, but we are primarily interested in the wavelength dependence). If the source has varied in the period between the two sets of observations, it is more likely to vary in flux (i.e. in normalisation), rather than having the peak wavelength vary (although we do note that the latter type of variation has also been observed – see, for instance, Pian et al. (1998)). The latter case would involve a change in the energetics of the emitting particles, and so would be less likely to occur on short timescales. Thus, the wavelength dependence of the polarisation should be the same for the two sets of data.

The second set of observations were made on the nights of October 12 – 14 1997, by the author and Michael Drinkwater. The sources presented here are those that are consistent with the sample definition given in Section 4.6: namely 0118−272, 0454+066 and 2210−257. We also observed 0118−272 and 0454+066 at optical wavelengths (using the ANU's 1m telescope), to obtain B, V, R and I magnitudes, since these were not observed in the sample of Francis et al. (2000). These observations were made during the three nights immediately preceding the AAT observations. 2210−257, on the other hand, is in the Francis et al. (2000) sample, and so we use that data for the modelling (this results in a difference of either 32 or 35 days between the photometry and the polarimetry). The reduction of the optical images was performed in the same way as described in Chapter 4.

6.4.2 Data reduction and measuring the polarisation

Each of the images made with *IRIS* were made up of multiple dithered 60 second images, each in turn made up of twelve averaged 5 sec exposures in H and K, and one 60 sec exposure in J. The initial part of the reduction was performed using FIGARO software specifically designed for the *IRIS* detector. This step accounted for the bias and dark current, and corrected for non-linearity between the number of photons incident on the chip and the number of electrons produced. The flat field was created from the difference of dome exposures with the lamps on and off – this removes any telescope emission, improving greatly the photometric accuracy. The effects of known bad pixels were removed by interpolating over them. The sky emission was removed by using a median of the five or seven data frames taken closest together in time. This median sky frame was then subtracted off the images to produce data frames with improved signal-to-noise. The resulting data frames were then aligned and median combined, to produce the final images. An example

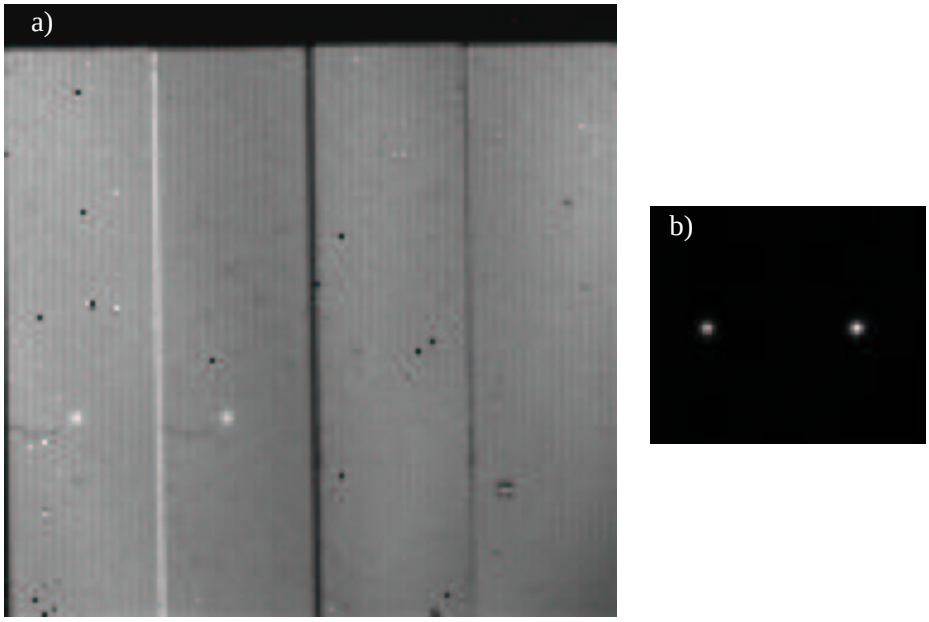

Figure 6.3: Example output from the *IRIS* detector, before and after reduction. a) The output from the whole chip, after bias subtraction and linearisation. Note the large number of bad pixels, as well as the noticeable structure in the sky background. b) The reduced image, showing just the source (0118−272) in two orthogonal polarisations. The polarisation of this source is noticeable in the different brightness of the two images (the right-hand one is brighter than the left).

of a single image after the linearisation stage (but before flat-fielding and bad-pixel removal) is shown in Fig. 6.3a, and the final image is shown in Fig. 6.3b.

The *IRIS* detector measures two orthogonal polarisations simultaneously, using a Wollaston prism. This prism produces two images next to one another on the detector, one in "ordinary" light and the other in "extraordinary" light (polarised in the direction orthogonal to the ordinary light). The chip actually has four images, two of a given part of the sky, and two of an adjacent part. For a given object, however, only two are of relevance. See Fig. 6.3a for an example.

From each of these two images, an intensity can be measured, giving I_1 and I_2. From these intensities we can find one of the Stokes parameters, say U:

$$U = \frac{I_1 - I_2}{I_1 + I_2}. \tag{6.2}$$

Thus, we can in principle find one of the Stokes parameters from a single

image. In practice, however, there will be some instrumental polarisation present. This can be removed by taking a second image with the plane of polarisation rotated by 90°(done with a half-wave plate located before the Wollaston prism). The ordinary and extraordinary images then swap positions on the chip, producing intensities I_1' and I_2'. We then use the "ratio technique"(from Frank Masci's Ph.D. thesis (Masci 1997)) to calculate the Stokes parameter without the effects of instrumental polarisation. First, we find the ratio

$$r = \sqrt{\left(\frac{I_1 I_2'}{I_1' I_2}\right)}, \tag{6.3}$$

and then calculate the Stokes parameter according to

$$U = \frac{r-1}{r+1} \tag{6.4}$$

The second Stokes parameter, Q, is measured in the same way, but with the plane of polarisation at 45°to the initial orientation. The total percentage polarisation (i.e. the fraction of the total light in the polarised component) is then given by

$$P = 100\sqrt{U^2+Q^2}\ \% \tag{6.5}$$

and its angle of orientation is given by

$$\theta_P = \frac{1}{2}\tan^{-1}\left(\frac{Q}{U}\right). \tag{6.6}$$

The errors in P are calculated assuming Poisson errors in the measured intensities I_1 etc. The resulting values $P \pm \sigma_P$ are listed in Table 6.1.

To find the photometry, each pair of ordinary and extraordinary images were added together, then all four summed images were combined to create the final image for each source and filter. The photometry was then performed with the *apphot* package in IRAF, using circular apertures with the sky background level determined by the median flux in an annulus around the source.

The photometry was calibrated with standard stars observed at the beginning and end of the night. These standard star observations, however, yielded differing flux levels across the different nights, and so the fluxes were bootstrapped from observations of the radio galaxy 2206−237 (on the basis

that this source was the least likely of those observed to have varied in the month since it was observed by Francis et al. (2000)). This provided NIR SEDs that were in better agreement with the optical SEDs from the observations a few nights earlier. The optical and NIR photometry for 0118−272 and 0454+066 are listed in Tables 6.2 and 6.3 respectively.

6.4.3 The modelling

Since the synchrotron component is the only polarised component, and its degree of polarisation does not change with wavelength, one would expect the percentage polarisation to be directly related to the amount of synchrotron flux present. In fact, the percentage polarisation will be directly proportional to the ratio of synchrotron flux to total flux. In Fig. 6.4, the polarisation of each of these quasars is plotted as a function of wavelength, together with the synchrotron ratio normalised (arbitrarily, as it is the wavelength dependence we are interested in, not the precise normalisation) to the K-band polarisation point (which is always the longest wavelength point). For completeness, a line of constant polarisation is shown, again normalised to the K-band point. All these sources are best fit with the combined model (see Appendix D for the model fits).

The fits to 0454+066 and 0118−272 were as follows:

- 0454+066: Best fit by the combined model, with $\chi^2_S/\nu = 3.08$ compared to $\chi^2_P/\nu = 5.92$. The synchrotron component had $\lambda_p = 0.66\mu$m, and a ratio of synchrotron to power law at 0.5μm of $R_{0.5} = 8.45$.
- 0118−272: Best fit by the combined model, with $\chi^2_S/\nu = 2.10$ compared to $\chi^2_P/\nu = 2.85$. The synchrotron component had $\lambda_p = 0.94\mu$m, and a ratio of synchrotron to power law at 0.5μm of $R_{0.5} = 1.10$.

Polarisation measurements from Wills et al. (1992) have also been included, where they exist. Once again, an allowance needs to be made for the fact that these observations were made without a filter. In a similar way as before, the mean wavelength for each object can be calculated:

$$\langle\lambda\rangle = \frac{\int \lambda f_T(\lambda)\mathrm{d}\lambda}{\int f_T(\lambda)\mathrm{d}\lambda} \tag{6.7}$$

The polarisation measurement is then plotted at this wavelength. These measurements are included with the caveat that they are *not* simultaneous

Source Name	$P \pm \sigma_P(\%)$			$P_{\rm opt}(\%)$ (Wills et al.)
	J	H	K	
0537−441	8.0 ± 0.5	8.7 ± 0.4	10.8 ± 0.8	—
0829+029	12.0 ± 0.4	12.5 ± 0.2	13.6 ± 0.1	8.2
1020−103	1.7 ± 0.2	2.5 ± 0.4	1.8 ± 0.6	0.6
1036−154	2.8 ± 1.3	3.1 ± 1.5	5.4 ± 2.0	—
1313−333	12.7 ± 0.3	12.9 ± 0.5	13.6 ± 0.5	—
1510−089	3.6 ± 0.2	—	2.7 ± 0.2	2.4
1546+027	6.2 ± 0.2	8.5 ± 0.2	8.6 ± 0.2	3.4
0118−272	17.2 ± 0.8	16.5 ± 0.5	17.0 ± 0.4	—
0454+066	5.1 ± 1.8	5.9 ± 1.0	2.9 ± 1.0	—
2210−257	3.4 ± 1.2	6.9 ± 1.5	4.0 ± 0.9	—

Table 6.1: Near-infrared polarisation measurements for ten PHFS sources, for the J, H and K bands. Errors given are 1σ. The data in the top section of the table are from the March 1997 observing run (Masci 1997), while the data in the bottom section are from the October 1997 run, detailed in the text. Also given are optical polarisation measurements from Wills et al. (1992).

Name	B	V	R	I
0118−272	16.59 ± 0.10	16.32 ± 0.10	15.89 ± 0.10	15.29 ± 0.10
0454+066	19.38 ± 0.13	18.74 ± 0.11	18.12 ± 0.10	17.45 ± 0.10

Table 6.2: Optical photometry of extra sources used for NIR polarimetry. The errors given are 1σ errors, with a 10% systematic error, as described in Section 4.5.

Name	J	H	K
0118−272	13.70 ± 0.10	12.79 ± 0.10	12.11 ± 0.10
0454+066	15.79 ± 0.10	14.95 ± 0.10	14.42 ± 0.10

Table 6.3: NIR photometry of extra sources used for NIR polarimetry. The errors given are 1σ errors, with a 10% systematic error, as described in Section 4.5.

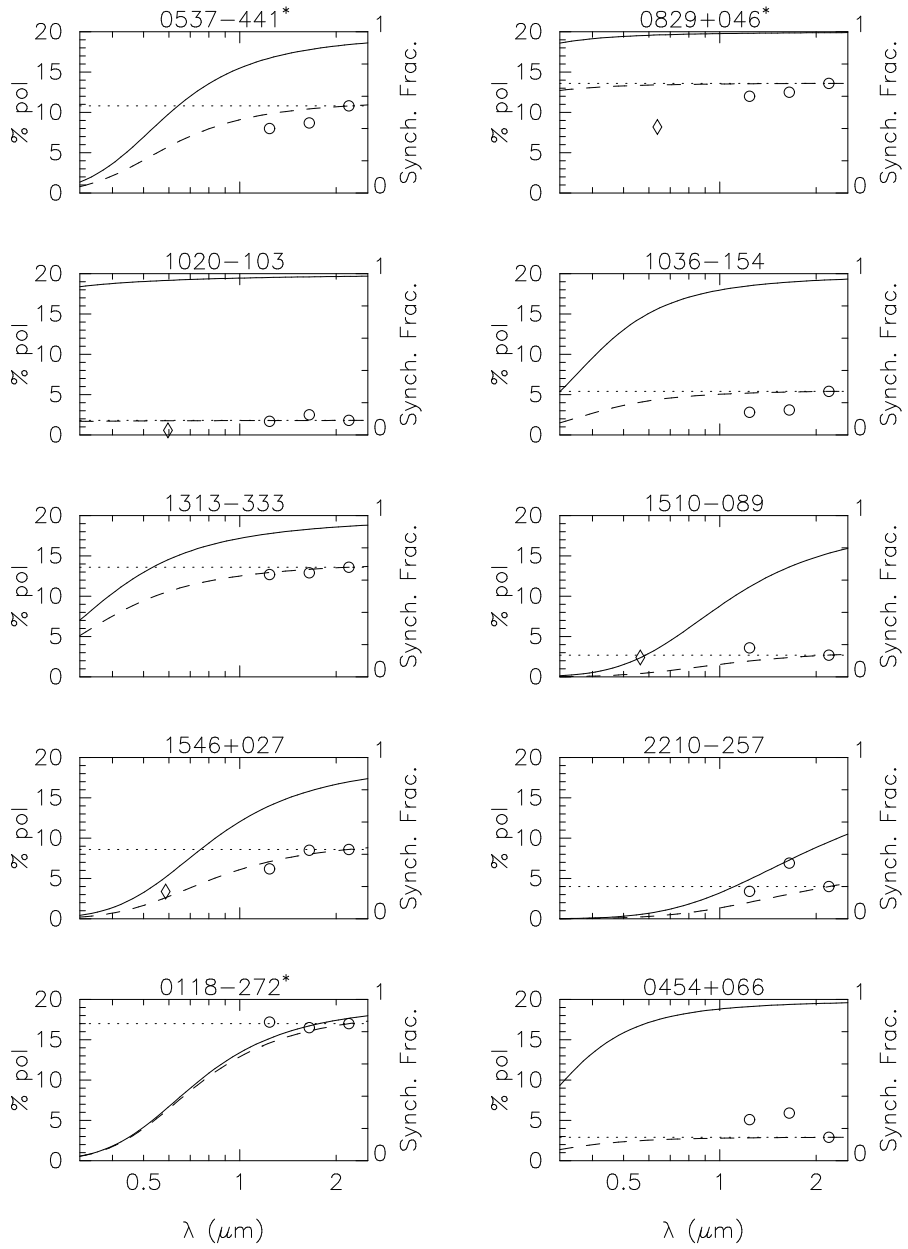

Figure 6.4: Near-infrared polarisation of a selection of quasars as a function of wavelength. Also shown are optical measurements from Wills et al. (1992) (plotted with a diamond). The solid lines show the fraction of the total flux made up by the synchrotron component (right-hand axis), while the dashed line shows this normalised (see text) to the K-band data point, and is in polarisation units (left-hand axis). The dotted line shows constant polarisation, normalised to the K-band data point as well. A * denotes the object is a BL Lac.

with the photometry (and hence the fitted model), nor with the NIR polarimetry. They are included merely as a guide, and should not be expected to agree with the fitted model.

The fitting gives mixed results for different sources. For some, such as 1546+027, the fitted synchrotron component replicates well the wavelength dependence of the polarisation. However, for some sources, such as 1313−333, the points are equally well given by a constant polarisation component. This is what you would expect from a pure synchrotron component, and these sources are typically BL Lac objects, from which you would expect to see a synchrotron-dominated SED.

A notable exception to this is the BL Lac 0537−441, whose polarisation is not fit well by a constant synchrotron component, but is fit better by a combination of a synchrotron and a significant power law component (although we do note that this source is suspected of having varied over the course of obtaining all the photometry observations – see Fig. 4.4 and Section 4.5 for a discussion of this variability).

Another source worth noting is 0118−272 (another BL Lac). Its polarisation appears to be better fit by a constant polarisation model, indicating a dominant synchrotron component. However, its optical SED (Appendix D) shows an upturn in flux at the blue end, leading to the fit of a strong power law component at short wavelengths.

It is apparent from these plots that having simultaneous optical polarisation measurements would better help discriminate between the combined model and a constant polarisation model. Unfortunately the NIR points by themselves do not provide enough wavelength range to distinguish the two models. The obvious next step in studying the polarisation of the PHFS sources would be to obtain simultaneous (or at least quasi-simultaneous) optical and NIR polarisation measurements of a number of sources, using *TAURUS* on the AAT in the optical, and either *IRIS2* (*IRIS'* replacement on the AAT) or *CASPIR* (on the ANU 2.3m) in the NIR (once they have polarimetry capability).

6.5 Summary

The optical and NIR polarisation properties of the PHFS quasars provides a very good way to test the fitted models from Chapter 5. Since the syn-

chrotron component is the only significantly polarised component in the modelling, one would expect the amount of polarisation at a given wavelength to be related to the amount of synchrotron emission present in the SED at that wavelength.

This is certainly supported by the correlation between the optical–NIR spectral index and the polarisation, where the redder sources have much larger polarisations than the blue sources. This can be interpreted as the redder sources having additional red, polarised emission over the top of the blue emission seen in the bluer sources. This qualitative analysis is realised in the combined model, where the polarised synchrotron component is added to a blue, unpolarised power law, making it redder. As an illustration of this point, see Fig. 5.8, where the combined sources have clearly redder power law slopes than the power law sources.

It is also seen that the amount of polarisation is related to the amount of synchrotron that is fit to the SED, so that the more highly polarised a sources is, the more synchrotron tends to be present in its spectrum.

Finally, by looking at the polarisation in different wave-bands, the wavelength-dependence of the polarisation can be deduced. For a number of sources, this is consistent with the predictions of the fitted models, however it was found that the wavelength range covered was a bit too restrictive to provide conclusive support (or otherwise) for the models. Optical polarisation measurements would thus be needed to make confident statements about the relationship between the models and the degree of polarisation.